Project FORTE - Nuclear Thermal Hydraulics Research & Development

Aerosol Dynamics in Sodium Cover Gas Region

August 2019

FNC 53798/48653R Issue 1

FRAZER-NASH CONSULTANCY

SYSTEMS AND ENGINEERING TECHNOLOGY

An introduction to Project FORTE

The Department for Business, Energy and Industrial Strategy (BEIS) has tasked Frazer-Nash Consultancy and its partner organisations to deliver the first phase of a programme of nuclear thermal hydraulics research and development.

Phase 1 of the programme comprises two parts:

- The specification and development of innovative thermal hydraulic modelling methods and tools; and
- The specification of a new United Kingdom thermal hydraulics test facility.

The work is intended to consider all future reactor technologies including Gen III+, small modular reactors and advanced reactor technologies.

Our project partners

The team is led by Frazer-Nash Consultancy and includes:

FRAZER-NASH
CONSULTANCY

The University Of Sheffield.

EDF ENERGY

Westinghouse

MANCHESTER 1824
The University of Manchester

Science & Technology Facilities Council

For more information, visit www.innovationfornuclear.co.uk/nuclearthermalhydraulics.html

Executive Summary

Liquid Metal Fast Reactors (LMFRs) are advanced nuclear reactor designs that are currently under development by the Generation IV International Forum for deployment in 10 to 20 years' time. LMFRs use liquid metal (e.g. sodium, lead or lead-bismuth eutectic) as the reactor coolant, allowing high power density with low coolant volume fraction and operation at low pressure. The designs make use of passive cooling to achieve a feature of inherent safety, and advanced fuel cycle to improve fuel efficiency and reduce waste.

An argon gas cover layer is often used in LMFRs above the liquid metal pool to prevent any air leakage into the vessel contacting the coolant, which creates a free surface above the pool. Due to the large temperature gradients across the gas layer, sodium evaporates from the free surface of the pool into the cover gas region where it condenses and forms a polydisperse aerosol. The evaporation and condensation process has an important effect on the heat transfer across the cover gas and the reactor operation. Therefore, heat transfer from the pool surface to the hot plenum roof is of significant interest in understanding the overall behaviour of the reactor. In addition, the deposition of sodium aerosol on the penetrations may be a safety concern including for fission-product retention under various fault conditions.

A multi-physics model has been developed to simulate the natural convection and heat transfer of the gas mixture together with aerosol dynamics in the cover gas region. The sectional method is employed for the general dynamics equation of the aerosol allowing for droplet growth by condensation, gravitational settling, Brownian diffusion and convection. This is coupled with the solution of the governing equations for continuity, momentum, energy and mass transfer for the gas mixture with the k-ω SST turbulence model.

This model simulated experiments conducted by Ohira in Japan in early 2000's and at the University of Manchester in the early 1990s to gain an understanding of the physics in the cover gas region. The major conclusions are as follows:

- The simulation results agree well with the experimental observations in terms of temperature distribution of the cover gas, heat flux through the roof and aerosol mass concentration. Significant differences between the simulation results and experimental data lie in the thermal boundary layer thickness over the top surface and the values of the roof heat flux, which may result from the deposition on the surfaces that occurred in the experiments.
- The droplets however do not follow exactly the large-scale structure of the gas mixture, but instead show smaller circulation cells as a result of gravitational settling. The simulation predicts significant accumulation of droplets above 20 µm radius at the bottom of the domain.
- The pool temperature appears to be a significant factor among these variables, whereas the roof heat flux increases only slightly as roof temperature decreases. A higher nucleation rate causes a higher aerosol concentration, but a lower roof heat flux.

A correlation of the aerosol mass concentration based on the experimental data and simulation results is presented for engineering applications.

The mathematical model has been implemented in Code_Saturne, an open-source finite volume code and therefore can be readily applied to other geometries and other setups of the cover gas region for LMFR designs. The initial development has demonstrated the potential of the model to simulate the aerosol distribution and temperature in the cover gas region, and so could be developed to support the design process.

Contents

1 Introduction

An essential feature of all Liquid Metal Fast Reactors (LMFRs) is the presence of an argon gas cover layer above the liquid metal pool to isolate it from the surroundings and allow for coolant volume changes when the operating temperature varies. The heat transfer from the pool surface to the roof is of significant interest to the understanding of the overall behaviour of the reactor, while the deposit of sodium aerosol on the components in the cover gas region may be a safety concern. Conversely, the free surface between the pool and cover gas is a source of argon gas entrainment to the sodium pool, causing various adverse effects. Despite the importance of the aerosol dynamics and heat transfer in the cover gas region, there is little knowledge documented in the open literature.

A series of measurements were made at the University of Manchester in the late 1980s [1] in order to determine the emittance of thermal radiation from a pool of liquid sodium under reactor temperature conditions and the emissivity of the stainless steels of interest in connection with sodium-cooled reactors. Subsequently, Anderson and Pei [2] carried out experiments with the sodium pool temperature varying over a range of 300 °C to 550 °C in a large scale liquid sodium pool test facility focusing on the complex heat transfer processes in the cover gas region. These experiments measured aerosol concentration and size distribution, cover gas temperature field, deposition rate of sodium on the side wall of the vessel and heat transfer rate to the roof [1], [2].

A research program named NACOWA (German acronym for sodium cover gas heat transfer) was launched in Germany from 1987-1993 to study parameters of the pool-type LMFR primary cover gas system under normal operation and design basis accident conditions [3]. Fifteen different NACOWA test series were carried out to investigate the enrichment of caesium, iodine, and zinc in the aerosol and in the deposits, and the difference between argon cover gas and helium cover gas. These tests measured the sodium aerosol characteristics and deposition on the cover plate, radiative heat transfer and the total heat transfer across the cover gas, sodium deposition on the cover plate and temperature profiles across the cover gas.

Work in Japan in the late 1970s concentrated on radiative heat transfer, mist transport and deposition in the aerosol-filled cover gas space. Kudo and Hirata studied sodium vapour deposition onto the cover plate [4], [5], while Furukawa performed an experimental study of a cylindrical enclosure above a sodium pool, and measured the temperature profile and aerosol mass concentrations with sodium pool temperatures ranging from 450 °C to 520 °C [6].

1.1 Objectives

The aim of the research described in this study is to develop a multi-physics model for the cover gas region aerosol dynamics and heat and mass transfer for Sodium-cooled Fast Reactors (SFRs). This report describes the development of the model and its validation against the experiments carried out at the University of Manchester in the early 1990s [1], [2]. A detailed discussion and a comprehensive understanding of the aerosol behaviour is presented, together with the heat and mass transfer in the cover gas region.

2 Methodology of modelling

The aerosol dynamics in which droplet sizes change due to condensation, evaporation, coagulation and chemical reactions are described by the so-called General Dynamic Equation (GDE). The GDE may be presented either in a discrete form, accounting separately for each cluster or droplet size in terms of the number of molecules that the cluster or size bin contains, or in a continuous form, wherein the distribution of droplets with respect to size is represented by a continuous function [7]. There are no general solutions to the GDE, although common methods used to solve the GDE for aerosol population include the modal method, quadrature method of moments, Monte Carlo method and sectional method [8].

- The sectional method provides an accurate description of the evolution of small clusters, for example, the initial formation of new droplets by homogeneous nucleation [7].
- The continuous method, e.g. the method of moments, assumes a distribution function for the polydisperse aerosol, which is natural for describing aerosols that include a broad range of particle sizes since the total number of cluster sizes that would be needed to describe aerosols extending to measurable sizes in the discrete form becomes immense [8].

The aerosol characteristics from the University of Manchester experiments [1], [2] demonstrate that the droplet diameter ranges from approximately 1 μm to 10 μm, indicating that the sectional method is suitable for the cover gas region.

Heat transfer across the cover gas occurs by radiation, convection and condensation, which determines the thermal load of the roof.

- The radiation flux has three different origins; radiation off the pool surface; radiation off the side walls; and reflected radiation that originates from the pool or side walls. The aerosol has a mitigating effect on the radiation across the cover gas, which is mainly scattering with a small amount of absorption. The emissivity used in this study for the metallic pool surface, side wall and roof were derived from measurements at the University of Manchester [1]. The absorption coefficient of the sodium aerosol-filled cover gas is obtained by correlating the experimental results of Hattori et al. [11].
- The mixed gas consisting of argon and sodium vapour naturally convects in the cylindrical region. The temperature difference between the roof and sodium pool surface varies from 300 °C to 400 °C, with the Rayleigh number being approximately 1.6×10^7 to 2.1×10^7, which is close to the demarcation between the soft and hard turbulence regimes [10].

The current study employs the k–ω SST turbulence model with two-scales wall function in Code_Saturne as a closure for the RANS equation, and efforts will be made to apply resolved Large Eddy Simulation (LES) modelling to the subsequent studies.

2.1 Governing equations

The cover gas region consists of a mixture of argon gas, sodium vapour and a fine mist of liquid droplets dispersed throughout the mixture. The temperature difference exerted on the top and bottom surfaces results in a density ratio of up to 1.67 and Rayleigh number ranging between 1.6×10^7 and 2.1×10^7. Therefore, the gas mixture is treated as a compressible ideal gas with variable thermophysical properties. The Reynolds averaged governing equations for the mixture are as follows:

Continuity equation for the mixture

$$\frac{\partial \rho}{\partial t} + \nabla \cdot (\rho \mathbf{U}_g) = -\Gamma \tag{1}$$

Momentum equation

$$\frac{\partial}{\partial t}(\rho \mathbf{U}_g) + \nabla \cdot (\rho \mathbf{U}_g \mathbf{U}_g) = -\nabla P + \nabla \cdot \mu[(\nabla \mathbf{U}_g) + (\nabla \mathbf{U}_g)^T - \frac{2}{3} tr(\nabla \mathbf{U}_g)\boldsymbol{I}] - \boldsymbol{F} + \rho \boldsymbol{g} - \nabla \cdot (\rho \overline{\boldsymbol{u}' \otimes \boldsymbol{u}'}) \qquad (2)$$

Energy equation

$$\frac{\partial}{\partial t}(\rho h) + \nabla \cdot (\rho h \mathbf{U}_g) = \frac{dP}{dt} + \nabla \cdot (\lambda \boldsymbol{\nabla} T) + Q - \mathit{\Gamma} c_p T \qquad (3)$$

Mass transfer equation for sodium vapour

$$\frac{\partial}{\partial t}(\rho Y_{\mathrm{Na}}) + \nabla \cdot (\rho Y_{\mathrm{Na}} \mathbf{U}_g) = -\nabla \cdot (\rho D_{\mathrm{Na}} \boldsymbol{\nabla} Y_{\mathrm{Na}}) - \mathit{\Gamma} \qquad (4)$$

where $\boldsymbol{F}$ is the drag force on the droplets, $\mathit{\Gamma}$ is the condensation rate of sodium vapour, Q is the latent heat release accompanying the phase change from vapour to liquid droplets. The species equation of Equation 4 is solved for the mass fraction of sodium vapour Y_{Na}, and the mass fraction of argon can be readily obtained as $1 - Y_{\mathrm{Na}}$. The Reynolds stresses are calculated using the eddy-viscosity *k–ω* SST turbulence model.

The equation of state is used to calculate the gas density of the mixture:

$$P = \rho R T \left(\frac{Y_{\mathrm{Na}}}{W_{\mathrm{Na}}} + \frac{Y_{Ar}}{W_{Ar}} \right) \qquad (5)$$

and density-based specific heat capacity is employed, while the viscosity and thermal conductivity are weighted by mole fraction.

The GDE is used for the evolution of aerosol populations due to the processes of Brownian diffusion, growth by condensation, convective transport and gravitational settling. The sectional method is applied to solve for the size distribution function n of the droplets. For the j^{th} cluster of droplets, the size distribution function is governed by the following equation:

$$\frac{\partial n_j}{\partial t} + \nabla \cdot (n_j \mathbf{U}_{p,j}) + \frac{\partial}{\partial r_{p,j}}(n_j \dot{R}_{p,j}) = \nabla \cdot (D_{p,j} \boldsymbol{\nabla} n_j) \qquad (6)$$

Droplets are convected by the gas phase, but also move relative to the gas due to gravitational settling. Therefore, the droplet velocity, $\mathbf{U}_{p,j}$, is composed of the gas velocity $\mathbf{U}_g$ and the settling velocity $\mathbf{U}_{G,j}$.

$$\mathbf{U}_{p,j} = \mathbf{U}_g + \mathbf{U}_{G,j} \qquad (7)$$

Considering the acceleration of a droplet under the action of gravity, the droplet's velocity after being released for a period t can be written as

$$\mathbf{U}_{G,j} = \mathbf{U}_{TS,j}[1 - \exp(-\frac{t}{\tau})], \; \mathbf{U}_{TS,j} = -\frac{2\rho r_{p,j}{}^2 \boldsymbol{g}}{9\mu} C_j \qquad (8)$$

where τ is the relaxation time by which a droplet can reach 63% of its terminal settling velocity $\mathbf{U}_{TS,j}$, and t is set to be the time step in the simulation. The thermophoretic velocity and diffusiophoretic velocity are ignored as their contributions are minimal compared to that of the gravitational settling [12]. C_j in Equation 8 is the Cunningham correction term:

$$C_j = 1 + \frac{l}{r_{p,j}}[1.257 + 0.4 \exp(-\frac{1.1 r_{p,j}}{l})] \qquad (9)$$

which is used to account for non-continuum effects when calculating the drag on small droplets.

The vapour-droplet interaction term $\frac{\partial}{\partial r_{p,j}}(n_j \dot{R}_{p,j})$ indicates the population evolution along the internal coordinate $r_{p,j}$ of the aerosol. In the continuum flow regime with Kn < 0.1 (Knudsen number defined as the ratio of the molecular mean free path length to the droplet diameter), the growth rate by condensation [13], [14] is:

$$
\begin{aligned}
\dot{R}_{p,j} &= \frac{D_{\mathrm{Na}} M_{\mathrm{Na}}}{\rho_p R T r_{p,j}} (P_{\mathrm{Na}} - P_{\mathrm{sat}}), \\
P_{\mathrm{Na}} &= P_{total} \frac{Y_{\mathrm{Na}}}{W_{\mathrm{Na}}} / \left(\frac{Y_{\mathrm{Na}}}{W_{\mathrm{Na}}} + \frac{Y_{Ar}}{W_{Ar}}\right) \\
P_{\mathrm{sat}} &= \exp(18.832 - \frac{13113}{T} - 1.0948 \ln(T) + 1.9777 \times 10^{-4} T)
\end{aligned}
\tag{10}
$$

In the free molecular flow regime where Kn > 10, a correction is needed based on the saturation vapour pressure of a flat surface P_{sat} taking into account that smaller droplets need a higher ambient relative humidity to maintain equilibrium than larger ones do, the growth rate therefore can be then given by [13], [14]:

$$
\begin{aligned}
\dot{R}_{p,j} &= \sqrt{\frac{M_{\mathrm{Na}}}{\rho_p{}^2 2\pi R T}} (P_{\mathrm{Na}} - P_D), \\
P_D &= P_{\mathrm{sat}} \exp\left(\frac{2\sigma M}{R T \rho_p r_p}\right)
\end{aligned}
\tag{11}
$$

In the transition regime (0.1 < Kn < 10), a harmonic mean of the expressions for the above two regimes is used.

Stokes-Einstein diffusivity is used as the Brownian diffusion coefficient in Equation 6:

$$
D_{p,j} = C \frac{RT}{N_A} \frac{1}{6\pi\mu r_{p,j}}
\tag{12}
$$

2.2 Model implementation and numerical methods

The above mathematical model is implemented in Code_Saturne, a general-purpose finite volume code developed at Électricité de France (EDF) R&D. The low-Mach number compressible solver has been used to solve the momentum, energy and mass transfer together with the continuity and state equation. The solution of the aerosol dynamics equations needs special treatment.

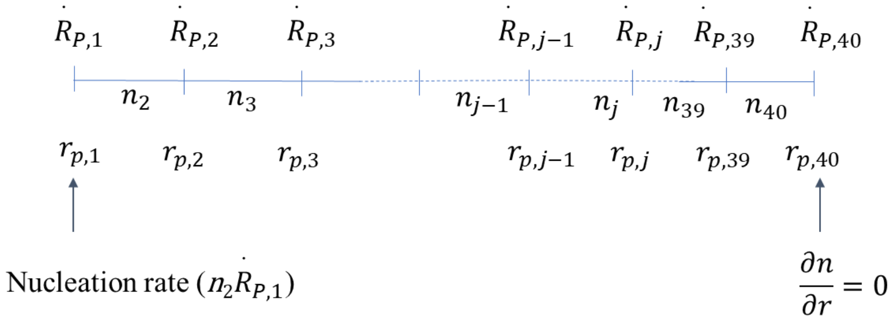

Figure 1: Division of the radius range

First, the size range of aerosol is divided into 40 bins (Figure 1) with the size distribution function defined on the mesh centre with respect to the internal coordinate r_p, and the aerosol growth rates defined on the boundaries. There are therefore 40 equations for the size distribution function, n_j, and these are re-cast in the form of a standard transport equation, as follows:

$$\frac{\partial(\rho n_j^{'})}{\partial t}+\nabla\cdot(\rho n_j^{'}\mathbf{U}_g)=\nabla\cdot(D_{p,j}^{'}\nabla n_j^{'})-\nabla\cdot(\rho n_j^{'}\mathbf{U}_G)-\frac{\partial}{\partial r_{p,j}}(\rho n_j^{'}\dot{R}_{p,j})+\nabla\cdot(D_{p,j}n_j^{'}\boldsymbol{\nabla}\rho) \quad (13)$$

The equations can then be solved using the Code_Saturne standard scalar solver. The term involving gravitational settling velocity is treated as a source term in addition to the source term of droplet growth by condensation.

The convective terms of Equations 1, 2, 3 and 6 are discretized by the second-order linear upwind (SOLU) scheme in Code_Saturne, whereas for the turbulence terms, first-order upwind is used [15]. The growth term of Equation 6 is discretized by a second-order central difference scheme in relation to the internal coordinate, droplet radius r_p. The SIMPLEC velocity-pressure algorithm is used for the momentum equation.

3 Ohira Test Case

A 2D model has been developed based on Ohira's experiments [12], [16] to facilitate the development of the numerical model and evaluate the uncertainties in it. This was then extended to a 3D model of the University of Manchester experimental rig (Section 4) to further validate the model and improve our understanding of the physics observed in the experiments.

3.1 Model setup

In the 2D model, the dimensions are the same as that of Ohira's study to facilitate the comparison between the simulation results of this study and the simulation results and experimental data in Ohira's work [12], [16]. The inner diameter and height of the apparatus are 0.588 m and 0.213 m respectively. Figure 2 shows the axisymmetric mesh arrangement of the 2D study and the monitored positions on the simulated domain.

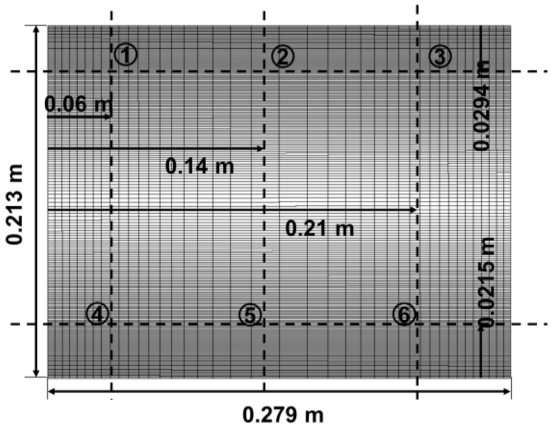

Figure 2: Mesh arrangement of the 2D model of Ohira's experiment and locations of the monitoring points

At the top surface of the simulated domain, temperature is fixed at the value of the tests, the number densities of the aerosol are set to be zero assuming deposition occurs on the roof and the mass fraction of the sodium vapour is set to saturated condition, i.e. assuming local equilibrium.

At the bottom surface of the domain, the pool temperature is set to be constant (at the value of the tests) and the sodium vapour is again set to its saturation value at this temperature assuming equilibrium. Neumann boundary conditions with spatial gradients of zero are applied for the number densities at the bottom of the domain.

The side wall of the 2D Ohira model is assumed to be adiabatic for the energy equation. Two different conditions for the mass fraction of sodium vapour and aerosol number densities are used to study the effects of deposition on the side wall: zero gradients for number densities and Y_{Na} when no deposition is considered, zero number densities and saturation condition for the sodium mass fraction when deposition is considered.

The minimum aerosol size under consideration is determined by the critical cluster radius as

$$r^{*} == \frac{2\sigma v_{m}}{k_{B} T \ln S} \tag{14}$$

where v is the molecular volume of the liquid.

Within the framework of classical nucleation theory, the nucleation rate *J* is given by

$$J = K\exp(-\Delta G k_B T) = \frac{P_{\mathrm{Na}} x_{\mathrm{Na}}}{k_B T}\sqrt{\frac{2\sigma}{\pi m}}\exp\left(-\frac{16\pi\sigma^3 m^2}{3(k_B T)^3 \rho_p^2 (\ln S)^2}\right) \tag{15}$$

Accordingly, the size range is determined as 0.001 µm to 50 µm. A constant nucleation rate is prescribed for the lower end of the droplet size, and a gradient of zero is defined as the upper boundary condition for the internal coordinate of the polydisperse aerosol. For the 3D simulation (Section 4.2), a homogeneous nucleation rate is considered in which the nucleation rate and the radius of droplets in the first size bin are determined by Equations 15 and 14 respectively.

3.2 Results and discussion

The 2D simulation of the Ohira rig was used to develop the numerical model and validate the results against the experimental data of average aerosol mass concentration and for evaluating the influence of different settings. Although the 2D model may not capture all of the physical effects, this approach enabled the methodology to be developed. The 3D simulation (Section 4) was then performed to study the physics of natural convection, aerosol formation and deposition at reactor operating conditions, providing comprehensive knowledge in addition to the University of Manchester experimental observations of the processes occurring in the cover gas region.

Unsteady simulations have been solved for the 2D study of the Ohira rig. In the 2D runs, the natural convection of the mixed gas is simulated alone before introducing the aerosol feedback. Fluctuations in temperature and velocity reach a steady oscillatory state in about 100 s as shown in Figure 3. From 150 s onwards, the aerosol is included in the simulation. The time step constant at 1×10^{-4} s is about 3 times the relaxation time in terms of gravitational settling of droplets with radius of 3 µm, indicating that droplets smaller than 3 µm can attain the terminal velocity within that time step, while the larger ones are still accelerating due to the imbalance between gravity and drag force. The maximum Courant number is approximately 0.0069 in this setting. Figure 3 shows the non-dimensional temperature evolution with time for the monitored locations (shown in Figure 2) in the Ohira model.

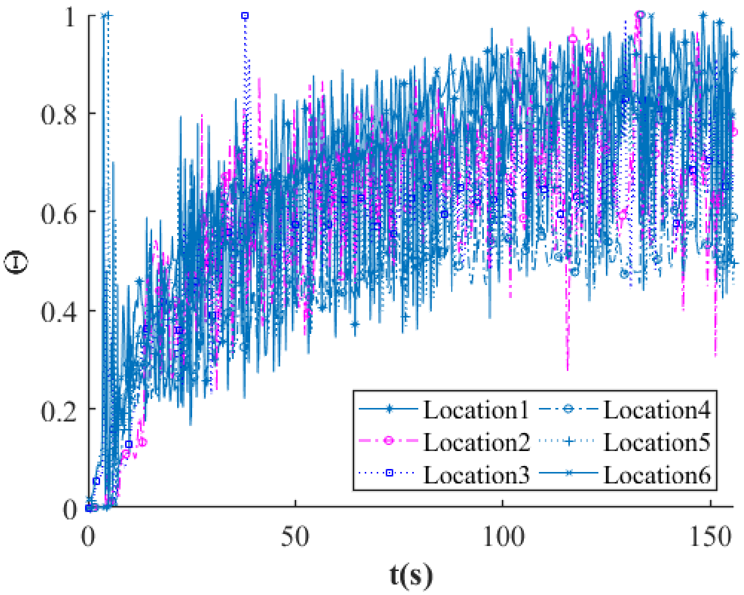

Figure 3: Temperature evolution with time for the monitored locations of Ohira rig

3.2.1 Convection of mixed gas and droplets

Figure 4(a) shows the temperature distribution together with the velocity vectors of gas mixture averaged over 100~150 s. A pair of large vortices occupy a large part of the domain. These vortices oscillate in the unsteady results. Additionally, small eddies appear and disappear periodically near the boundary walls.

Fluctuations also appear in the temperature, velocity and mass concentration of the aerosol in the unsteady results with aerosol influence after 150 s of simulation. Figure 4(b) illustrates the temperature and velocity distributions of the mixed gas with droplet-gas interaction averaged over 200~250 s. The flow domain is now dominated by a large circulation and a small eddy close to the top cover. The maximum velocity decreases from 0.436 m/s in Figure 4(a) to approximately 0.37 m/s in Figure 4(b), which can also be attributed to the drag force between the dispersed phase and the continuous phase.

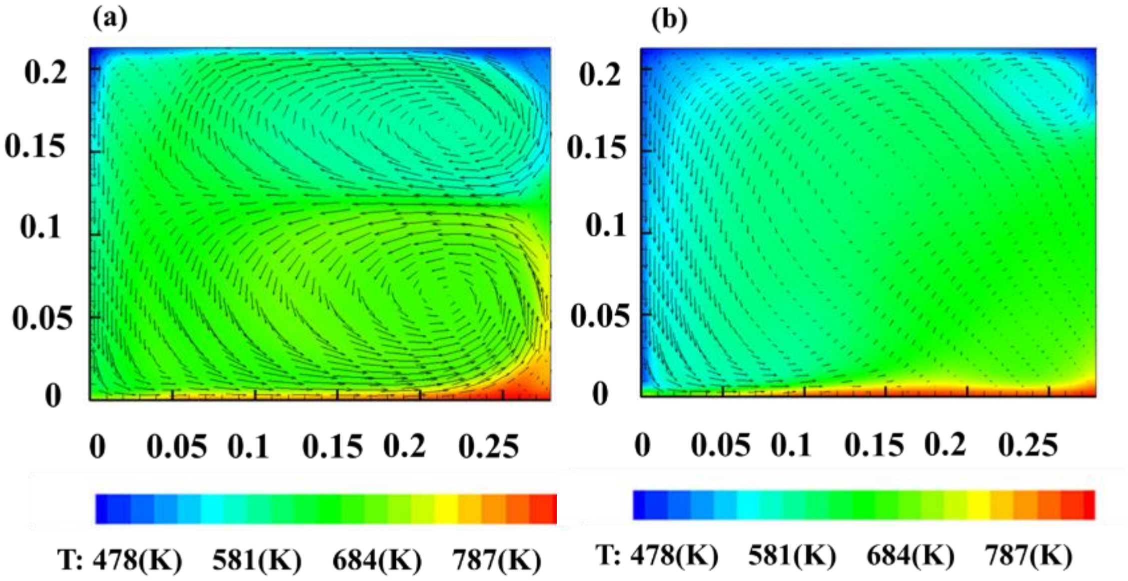

Figure 4: Averaged temperature contour and velocity vectors of gas mixture for (a) 100~150 s and (b) 200~250 s

3.2.2 Temperature distribution and mass concentration of aerosol

Five cases are run to evaluate the sensitivity of the model to different settings (Table 1). Cases 1 and 2 are compared to identify the best value of nucleation rate in the simulation. Cases 3 and 4 include thermal radiation using the discrete ordinates method in Code_Saturne with the directions for angular discretisation being 24 directions (S4). The emissivities of the surfaces are derived from experiments as 0.65 for the top surface, 0.45 for the side wall and 0.04 for the bottom surface.

In Case 3, the whole cover gas region is treated as a transparent medium, whereas in Case 4, the absorption coefficient is specified uniformly as 0.3. This value was chosen to test the sensitivity of the results to absorption coefficient. This is investigated further in the 3D model (Section 4.3) by using non-uniform distributions of absorptivity.

The deposition rate on the side wall was reported to be less than 10% of the total removal rate [1] when the pool temperature is 550 °C. Thus in Case 5, it is assumed that any aerosol reaching the side wall is deposited on it (hence takes account of the deposition on the side wall by setting the aerosol number densities to be 0) and keeping it at the state of fully saturated with sodium vapour through adjustment of Y_{Na}.

Case No.	T_{pool} (°C)	T_{roof} (°C)	Nucleation rate ($cm^{-3}\cdot s^{-1}$)	Deposition on side wall	Absorption coefficient (m^{-1})
1	531	205	200	N	N/A
2	531	205	35	N	N/A
3	531	205	35	N	0
4	531	205	35	N	0.3
5	531	205	35	Y	N/A

Table 1: Cases 1-5 for the Ohira rig

Figure 5 compares the average aerosol mass concentrations from simulations to the experimental observations. The results of the simulations are sensitive to the nucleation rate and suggest that the nucleation rate of 35 $cm^{-3}\cdot s^{-1}$ in Case 2 is predicted to be more suitable for this configuration than that in Case 1. The results also show that the aerosol concentrations in Cases 2 to 5 all fall within a reasonable range compared to the experimental results, and the aerosol concentration is not particularly sensitive to the model settings in those simulations.

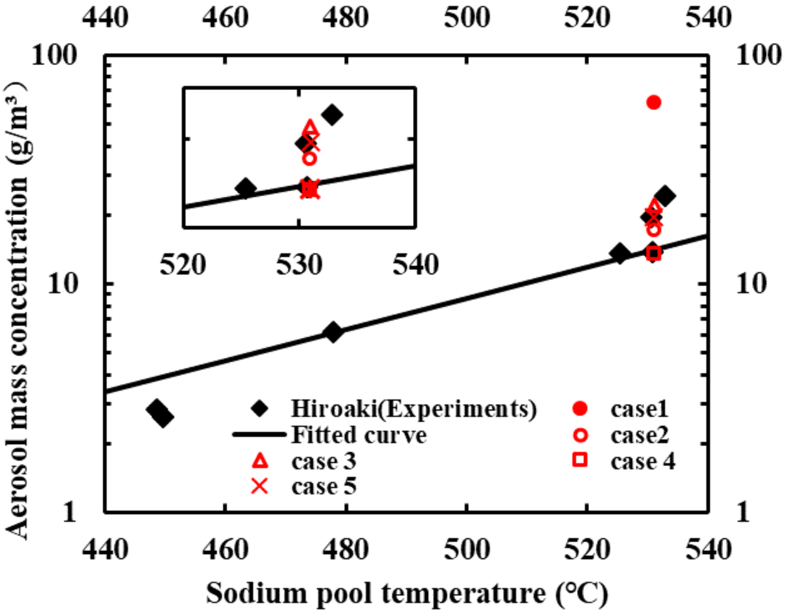

Figure 5: Aerosol mass concentrations in Cases 1 to 5 and experimental data from References [12], [16]

Figure 6 compares the temperature distributions with and without radiation. The inclusion of radiation between surfaces in Case 3 induces a more uniform temperature distribution compared to the results of Case 2 (no radiation). However, in Case 4, where the aerosol is considered as a semi-transparent medium with an absorption coefficient of 0.3, the temperature profile consists of two large vortices which is similar to that without aerosol shown in Figure 4(a).

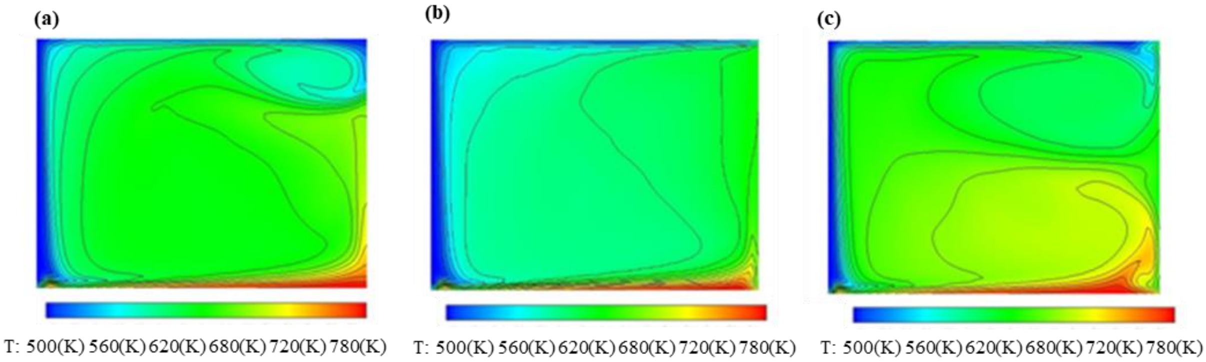

Figure 6: Averaged temperature distribution of (a) Case 2; (b) Case 3; (c) Case 4

The differences in temperature distribution in Figure 6 can be attributed to the incident flux: the radiant flux from the bottom surface to the top surface results in a smoother vertical temperature distribution in Case 3 compared with that in Case 2. With an absorption coefficient of 0.3 in Case 4, the intensity of radiation decreases linearly with distance from the bottom surface, thus the influence of radiation is more intensive in the lower part, which could cause the two vertically distributed vortices in this case. The correlation between absorption coefficient and aerosol concentration is investigated in the 3D model (Section 4.3).

As illustrated in Figure 7, allowing deposition on the side wall induces a lower concentration of sodium vapour in Case 5 compared to that in Case 2 and therefore a smaller growth rate of aerosol. Although the relative humidity is lower in Case 5, the aerosol mass concentration is slightly higher than Case 2. This is explained by the discrepancy in number density of the nucleation sites: given that the nucleation rate is the same in both cases but the growth rate is lower in Case 5 the spatially-averaged number density of nucleation sites in Case 5 is 3.25×10^{6} m^{-3} compared to 1.79×10^{6} m^{-3} in Case 2. The nucleation rate depends on the nucleation mechanism and operation conditions of the experiments, and so is a calibrated parameter in the simulation.

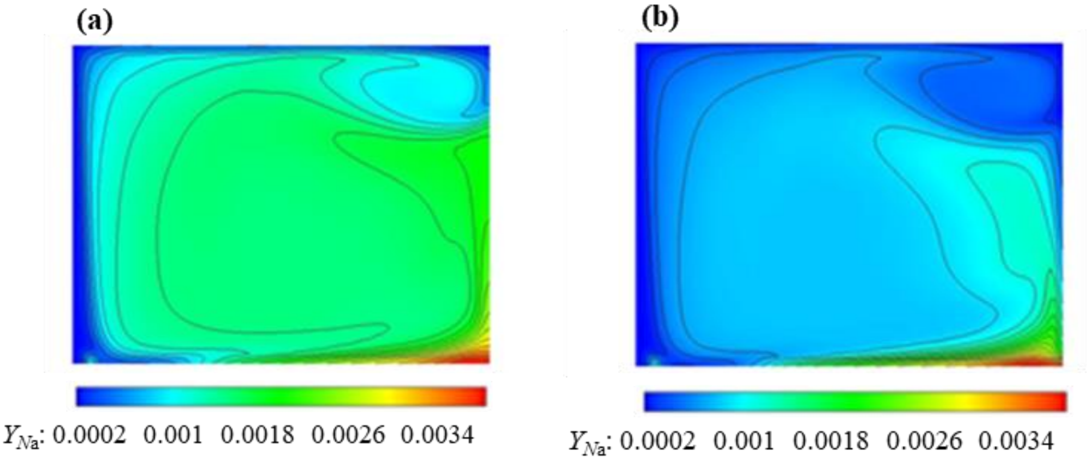

Figure 7: Averaged mass fraction of sodium vapour in (a) Case 2 and (b) Case 5

4 University of Manchester Test Case

4.1 Experimental apparatus

The MUSAC3 (Manchester University Sodium Aerosol Characteristics) rig consists of a main test section with a sodium pool in the bottom and an argon cover gas space above it. Figure 8 shows the sodium pool test section, which is an 800 mm diameter cylindrical stainless-steel vessel with a wall thickness of 6 mm and height varying from 320 mm at the shallow end to 390 mm at the deep end. The bottom surface of the test section is inclined to allow it to be drained whilst the rig is not in operation. In addition, a sodium supply and storage system are provided to facilitate the filling and draining operations, and an argon circulation and supply system is provided for filling the cover gas space.

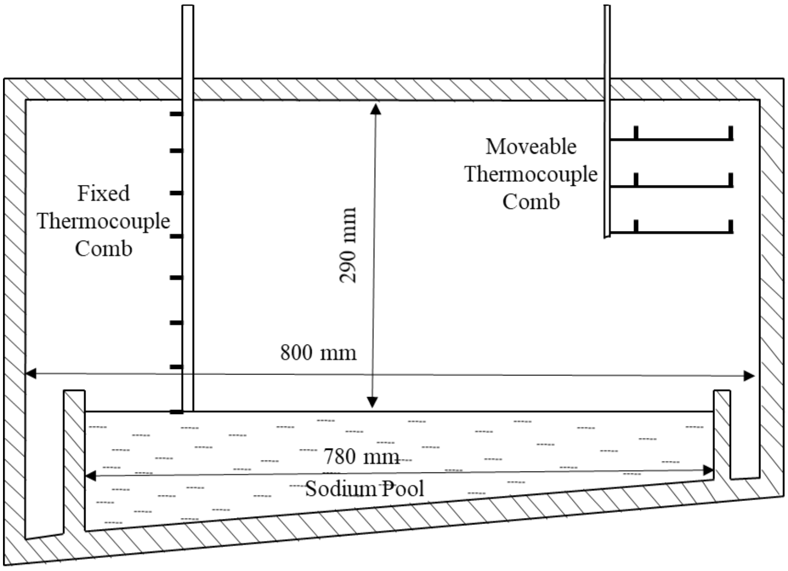

Figure 8: Schematic diagram of the sodium pool test section of the MUSAC3 rig

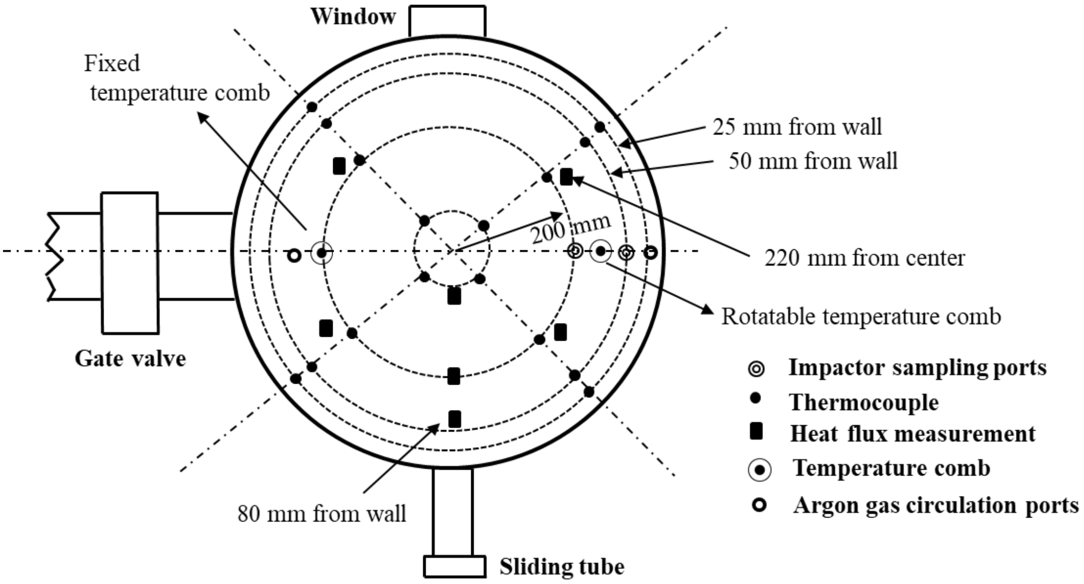

Figure 9: Locations of heat flux sensors, thermocouples and sampling ports on the roof

On the roof of the test section, there are six penetrations arranged on one plane as shown in Figure 9. Two of the penetrations are used as inlet and outlet ports for cover gas circulation; two sampling ports (one at a radius of 200 mm from the centre and the other 50 mm from the wall) for the Anderson Jet Impactor, which is used for measuring the aerosol characteristics; the remaining two are used for the thermocouple combs. A rotatable thermocouple comb, which can be moved vertically is inserted into the test section through the roof above the shallow end of the sodium pool. Another fixed thermocouple comb is provided which is located above the deep end of the sodium pool for measuring the temperature profile in the vertical direction. The thermocouples are stainless sheathed and mineral insulated K-type thermocouples, and heat transfer rate through the roof is measured.

4.2 Model Setup

Figure 10 shows the 3D model for the University of Manchester rig together with the mesh arrangement and dimensions. The sodium pool test section is a cylindrical vessel with a diameter of 800 mm, a height of 320 mm at the shallow end and 390 mm at the deep end. A structured mesh is employed for the simulation. A refined node distribution is used near the boundaries with a coarser distribution near the centre. The total number of volumes is 0.46 million and the y+ of the first nodes near the wall is kept below 1.

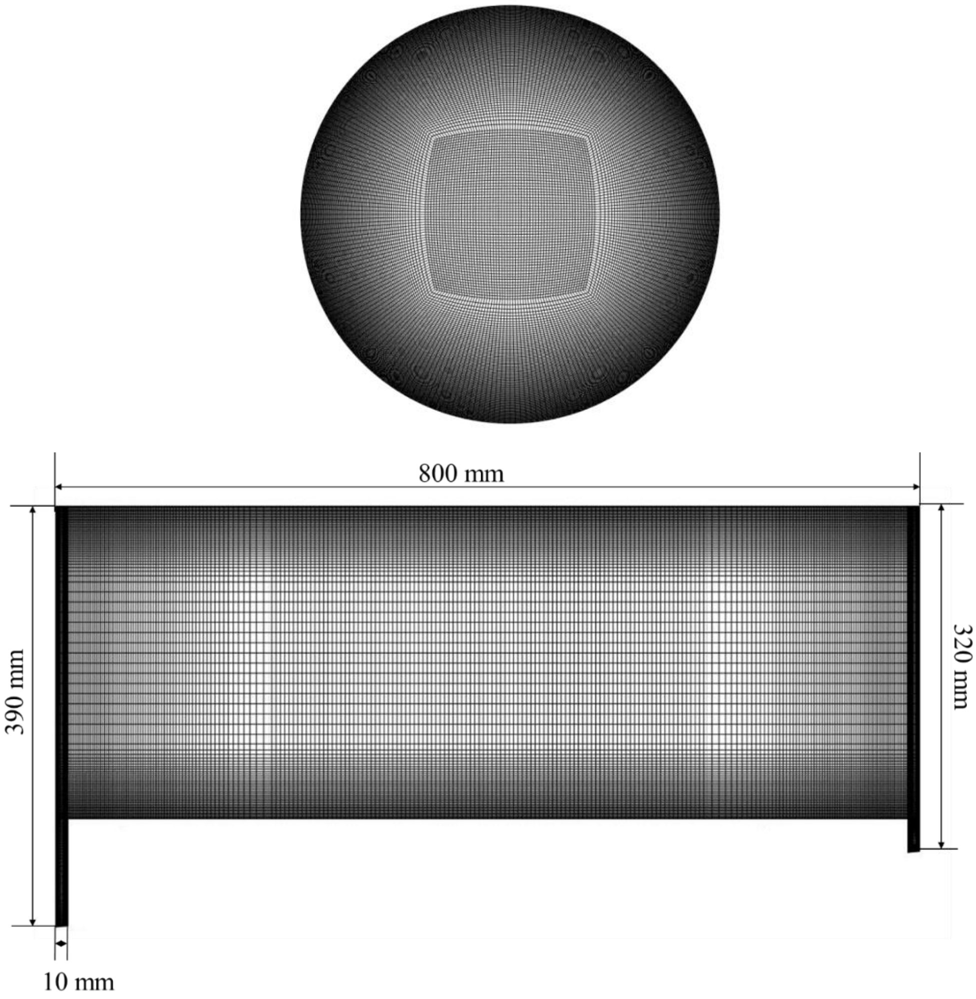

Figure 10: Mesh arrangement on the top surface and the slice through the centre of the 3D model

As with the Ohira test case, the temperature of the top surface of the simulated domain is fixed at the value of the tests. In the Manchester experiments, a number of air cooling fans are mounted 1m above the roof of the test section to maintain a uniform temperature. The number densities of the aerosol are set to zero assuming deposition occurs on the roof, and the mass fraction of the sodium vapour is set to saturated conditions, i.e. assuming local equilibrium.

At the bottom surface of the domain, the pool temperature is set to be constant (at value of the tests) and the sodium vapour is again set to its saturation values at this temperature assuming equilibrium. Neumann boundary conditions with spatial gradients of zero are applied for the number densities at the bottom of the domain.

Deposition on the side wall is not considered (i.e. zero gradient is used), and a constant wall temperature is specified as a water jacket was used to keep the side wall temperature to be the same as the cover gas temperature in the experiments.

At the present time, only steady flow simulations have been carried out for the full 3D study of the University of Manchester rig.

4.3 Results and Discussion

Eight steady-state simulations have been carried out to investigate the effects of different settings as shown in Table 2. In accordance with the experimental setup, two series of boundary conditions are applied. The roof temperature is set to either 160 °C or 200 °C, whilst the pool surface temperature is fixed at 550 °C. The side wall temperature is kept at the bulk temperature of the cover gas.

Cases 1 and 2 are base cases for a roof temperature of 200 °C and 160 °C respectively, Cases 3 and 4 ignore the effect of the drag of the aerosol on the mixture flow, and Cases 5 and 6 include the effect of thermal radiation across the aerosol-filled cover gas space. The absorption coefficient of the sodium aerosol-filled cover gas is obtained by correlating the experimental results of Hattori et al. [11].

$$\alpha = 0.0828 + 0.642 C_{\mathrm{A}} \tag{16}$$

where C_{A} is the aerosol concentration with unit of g/m^3.

In order to study the influence of nucleation mechanisms, Case 7 uses a nucleation rate that is twice the value used in Cases 1 to 6, and Case 8 assumed homogeneous nucleation with the nucleation rate determined by Equation 15 in the simulation.

Case No.	Tpool (°C)	Troof (°C)	Aerosol feedback	Absorption coefficient	Nucleation rate (cm^{-3}·s^{-1})
1	550	200	Y	N/A	50
2	550	160	Y	N/A	50
3	550	200	N	N/A	50
4	550	160	N	N/A	50
5	550	200	Y	Equation 16	50
6	550	160	Y	Equation 16	50
7	550	160	Y	Equation 16	100
8	550	160	Y	Equation 16	Equation 15

Table 2: Settings for Cases 1 to 8 for the University of Manchester rig

4.3.1 Convection of mixed gas and droplets

A quasi-two-dimensional roll-like structure is observed in the simulations of Cases 1 to 6. A principal plane can be identified which has the largest and strongest circulation cell on it, whereas on the plane normal to that, several vortices with smaller peak velocities appear instead. For instance, the maximum velocity of the main flow structure is up to 0.35 m/s in Case 6, while the flow perpendicular to it is much weaker with velocities up to around 0.15 m/s. The location of the principal plane is not fixed and varies with different temperature boundary conditions.

Figure 11 shows the circulations in Case 5 and Case 6. The coordinate system is defined so that the y-axis is along the line from the deep end to the shallow end of the pool, and the x-axis and z-axis are normal to it. The main flow structure in Case 5 lies on the plane with a normal vector n being [cos(π /6), sin(π /6), 0], whereas in the cases with a roof temperature of 160 °C, n of the principal plane with the main flow structure is [cos(- π /18), sin(- π /18), 0]. This flow pattern is supported by the experiments as the temperature and heat flux measured on one side of the test section were generally higher than those measured on the other side, which suggests that there is a large, dominating circulation in the region and the flow is not symmetric.

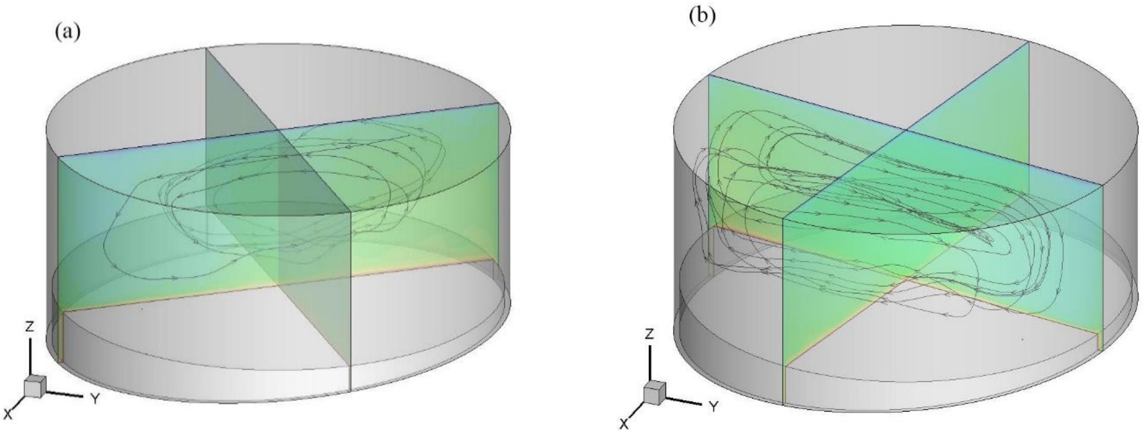

Figure 11: Cover gas circulation patterns in (a) Case 5 with roof temperature of 200 °C and (b) Case 6 with roof temperature of 160 °C. Selected streamlines are shown, the principal and orthogonal planes are coloured by temperature

As an illustration of the natural convection of the gas mixture and transport of the poly-dispersed aerosol, Figure 12 and Figure 13 show the velocity distributions of gas mixture and droplets of different sizes in Case 5 on the principal planes shown in Figure 11(a) through the centre (0, 0, 0) of the domain.

Figure 12 shows the velocity profiles of the gas mixture on the principal plane and the orthogonal plane to that. A large structure is developed on the principal plane, whereas a few vortices with much smaller velocities are formed on the plane orthogonal to it.

Figure 13 shows the trajectories of droplets with radii of 0.6 μm and 40.6 μm on the principal plane. The larger droplets do not follow the gas exactly due to gravity. In contrast to the large structure of the gas mixture, the mist of such large droplets shows a pattern of smaller vortices. With the increase of droplet size, the tendency of a downward flow becomes more significant as the heavy droplets tend to accumulate at the bottom.

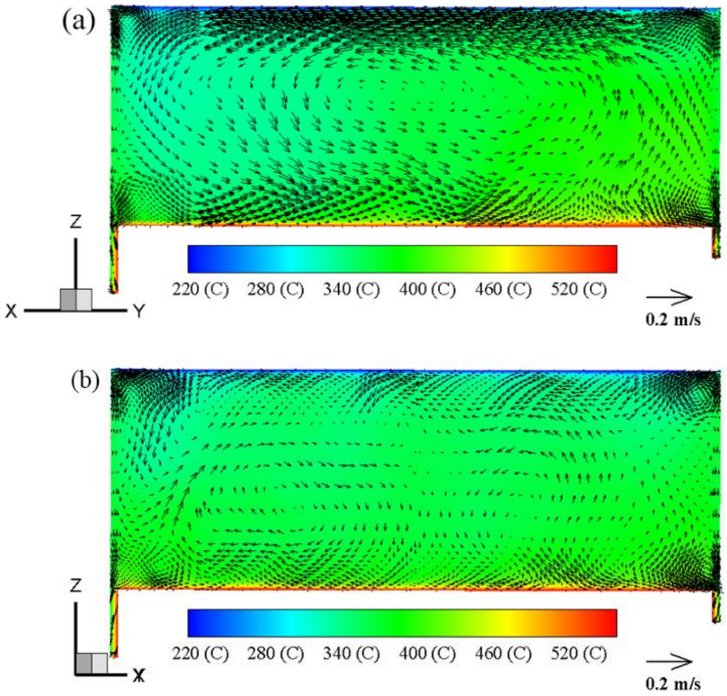

Figure 12: Temperature and velocity distributions of gas mixture on (a) the principal plane (b) the orthogonal plane to the principal one in Case 5 (roof temperature of 200 °C)

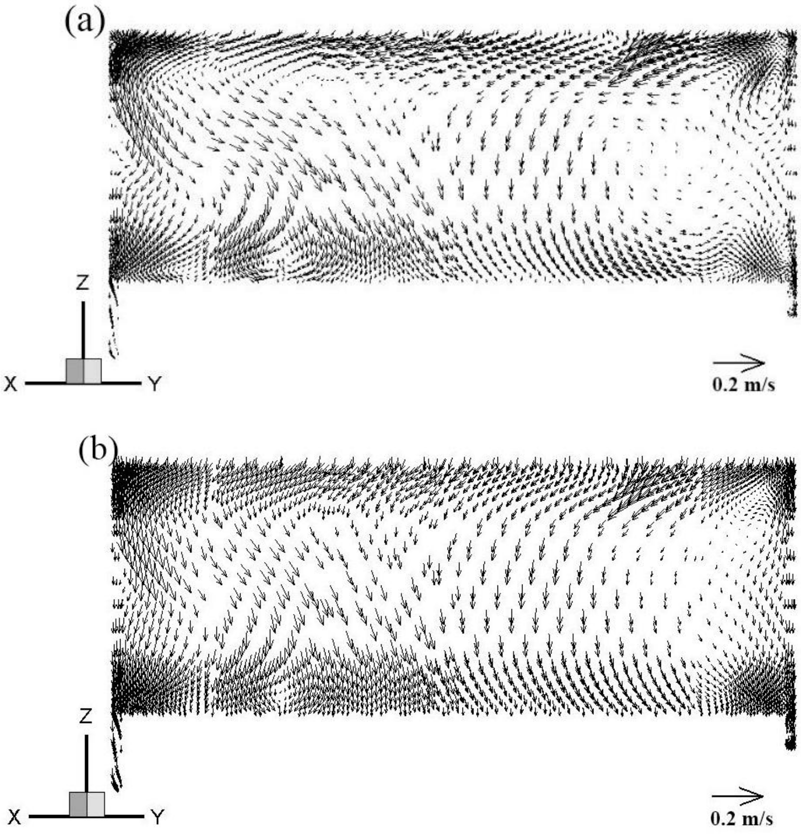

Figure 13: Velocity distribution of droplets with radius of (a) 0.6 µm and (b) 40.6 µm on the principal plane in Case 5 (roof temperature of 200 °C)

4.3.2 Temperature distribution and heat flux through the roof

The vertical temperature profiles were obtained using the moveable thermocouple comb in the experiments at 170 mm from the cylinder centre. Figure 14 shows the measured and simulated temperatures for roof temperatures of 160 °C and 200 °C. Cases 3 and 4 are without aerosol feedback to serve as base cases for comparison. The temperature profiles generated by Cases 1 and 2 with aerosols agree well with the experimental data except in the thermal boundary layers at the top and the bottom.

The boundary layer thicknesses in Cases 1 and 2 are about half that observed in the experiments. The discrepancy between the simulation and experiment increases with a larger temperature difference between the roof and the pool. In Cases 5 and 6 with radiation taken into consideration, the thermal boundary layers become slightly thicker as a result of the absorption of the thermal radiation. The increase of thickness is more significant at the bottom than that at the top due to the non-uniform distribution of absorption coefficient and the fact that radiation is stronger at the bottom.

The condensation and deposition of aerosol on the roof surface, which would create a sodium layer on the surface and deteriorate heat transfer, may lead to a thicker thermal boundary layer in the experiments. This could account for the differences in temperature distribution at the top surface between the experimental data and simulation results. It was observed in experiments that film wise condensation took place on the roof when the top surface temperature was above 200 °C, while drop wise condensation occurred below this temperature, suggesting that the influence of condensation on the top surface varies with roof temperature.

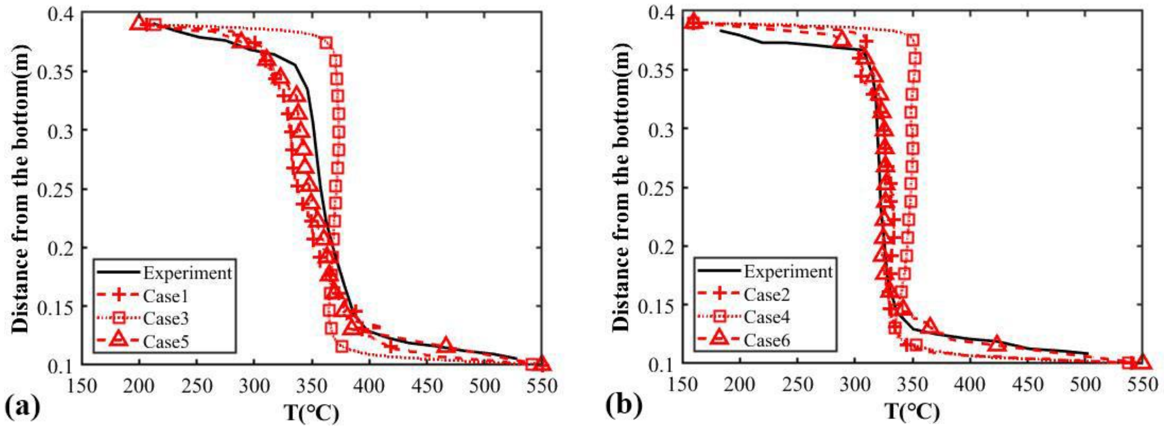

Figure 14: Comparison of temperature profiles for pool temperature of 550 °C, roof temperature of (a) 160 °C and (b) 200 °C (Experimental data from Anderson and An [1], [2]. The pool surface is 0.1 m from the bottom of the domain

Figure 15 shows the simulation results of the heat flux under various conditions and theoretical predictions of the roof heat flux as a function of pool temperature for roof temperatures of 120 °C and 160 °C in An's work [1], together with experimental results obtained using the heat flux sensors on the roof and the calorimetric method by Anderson and An [1], [2]. In the theoretical approach, energy conservation in terms of radiosities and irradiances were formulated for four elemental surface regions, namely the roof centre, roof edge, upper wall and lower wall by calculating the view factors using the Monte Carlo method [1].

In the experiments, local values were measured directly by the heat flux sensors or the calorimetric cooling system. A radial heat flux distribution was derived by interpolation based on the measurements of the seven heat flux sensors on the roof, an area-averaged roof heat flux was then obtained through integration of the radial distribution. The calorimetric method took the average of heat flux values at 36 evenly spaced locations measured directly by the calorimetric cooling section.

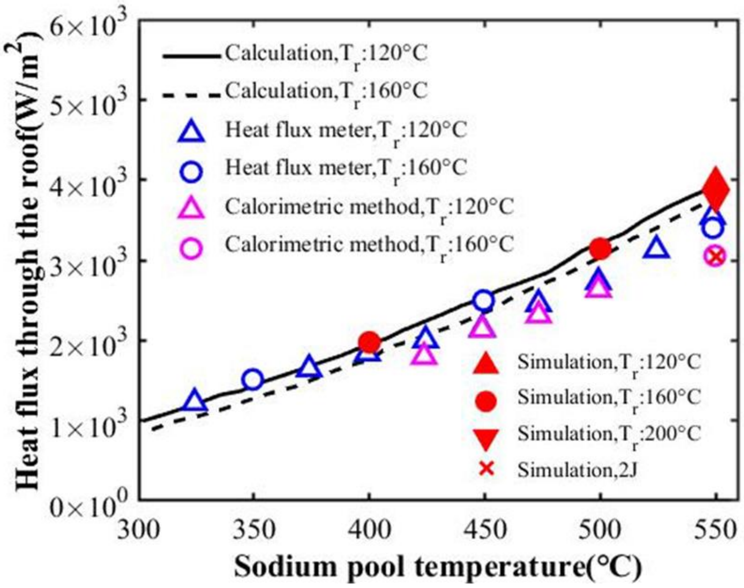

Figure 15: Impact of roof and pool temperature on heat flux through the roof (Experimental data and calculation results from Anderson and An [1], [2])

The comparison in Figure 15 shows that for a pool temperature above 400 °C, theoretically predicted values are higher than the experimental data. This is probably because the sodium aerosol is sufficiently dense at high pool temperatures and the distribution of droplets is non-uniform as implicated by Figure 13, whereas the theoretical model assumed a uniform distribution of a semi-transparent cover gas. The simulation results are also generally higher than the experimental results and the discrepancy increases with the pool temperature. This may be explained by the decrease of the surface emissivity when deposition occurs in the experiment, and the decrease is non-uniform on the surfaces as deposition may be stronger at the corner compared to that at the centre.

For a pool temperature of 550 °C and roof temperature of 160 °C, the present CFD simulation result is 13% higher than the results obtained by the heat flux sensors and about 22% higher than the calorimetric results, while it is 4% higher than the calculation result. The value of the heat flux increases significantly with pool temperature while it decreases slightly with the roof temperature as demonstrated by the simulation results at a pool temperature of 550 °C.

A sensitivity simulation was carried out (Case 7) with the nucleation rate doubled to test the influence of *J*. The heat flux decreases by 22% with 2*J* as shown in Figure 15, which arises from the higher degree of attenuation of radiation through the mist with a denser aerosol. The simulation results show that thermal radiation accounts for approximately 75% of the total heat flux through the roof for a pool temperature of 550 °C, and the percentage increases to around 80% at a pool temperature of 400 °C as a result of the decrease in the Nusselt number and less absorption by the mist.

This high degree of thermal radiation suggests that the prediction of the roof heat flux depends substantially on the accuracy of the calculation of thermal radiation, thus uncertainties in the simulation of radiation, such as the uneven distribution of emissivity on the surfaces and the influence of semi-transparent aerosol, deserve further investigation.

4.3.3 Aerosol characteristics

Figure 16 shows the distribution of the aerosol number density for droplets with radii of 1.9 µm, 20.6 µm and 40.6 µm on the principal plane in Case 5. For droplets of r_p =1.9 µm (Figure 16a), nucleation occurs at the top surface where the sodium vapour is supersaturated with high relative humidity on the roof. For the medium size bin, 20.6 µm (Figure 16b), droplets are convected by the gas mixture and simultaneously fall towards the pool surface due to the downward force of gravity. Therefore, the number density is generally higher on the side where the gas mixture flows downwards compared to that on the other side and the layer of droplets on the roof disappears. As for the large size bin, 40.6 µm (Figure 16c), an accumulation of droplets close to the bottom surface arises and droplets hardly exist near the roof.

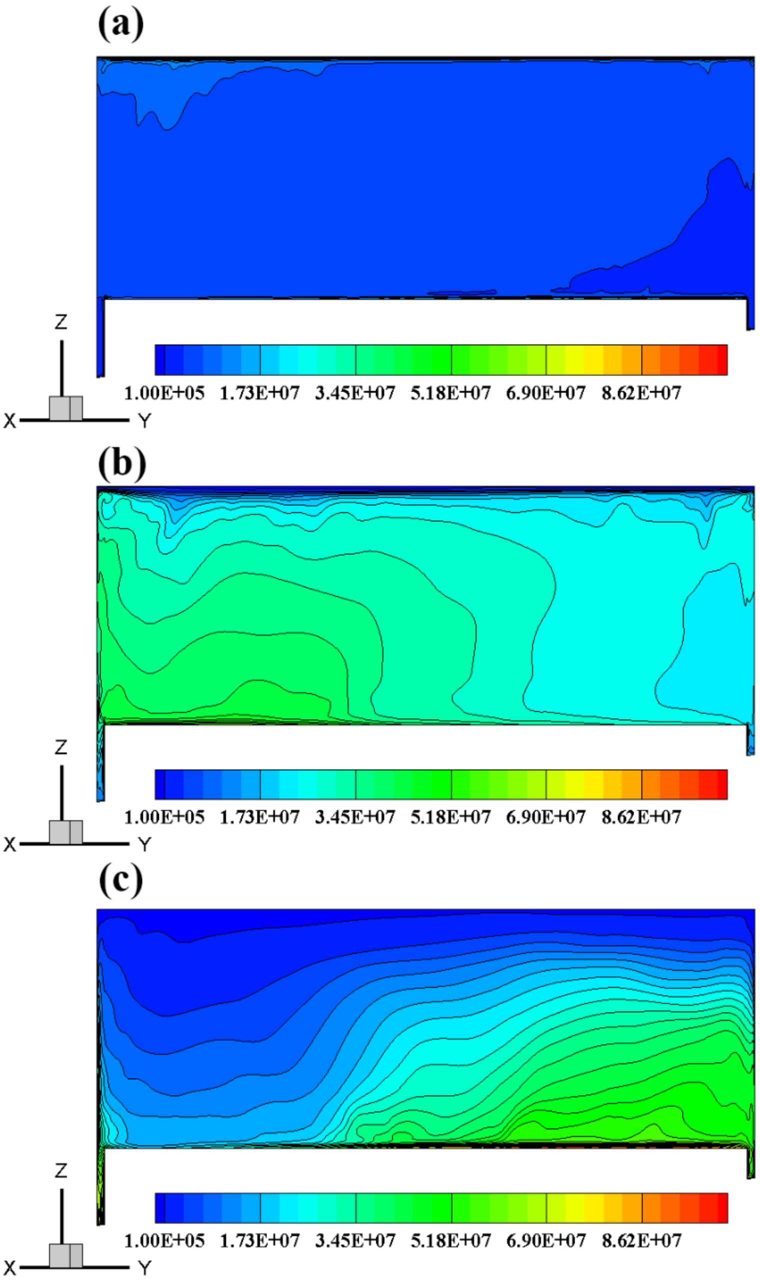

Figure 16: Number density distributions of droplets with radius of (a) 1.9 µm, (b) 20.6 µm and (c) 40.6 µm on the principal plane in Case 5

Figure 16 shows that the smallest droplets exist with a relatively low concentration throughout the cover gas region, while the larger ones do not exist near the roof or downward flow region as they are heavier and difficult to lift by the convection flow. These phenomena are also implied by the velocity profiles of the droplets in Figure 13. The downward movement of aerosol observed on the principal plane also exists on the plane orthogonal to it, except that the distribution of vortices of the mixture and the aerosol appear to be largely symmetric on that plane.

The aerosol characteristics are extracted at six locations on the principal plane (Figure 17) to better understand the aerosol size distribution. Locations 1-3 are 80 mm below the top surface, while Locations 4-6 are 80 mm above the pool surface. The radial positions of the locations are -0.35 m, 0 m and 0.35 m respectively. Figure 18 and Figure 19 show droplet velocities and number density distributions against droplet radius at Locations 1-6 in Figure 17.

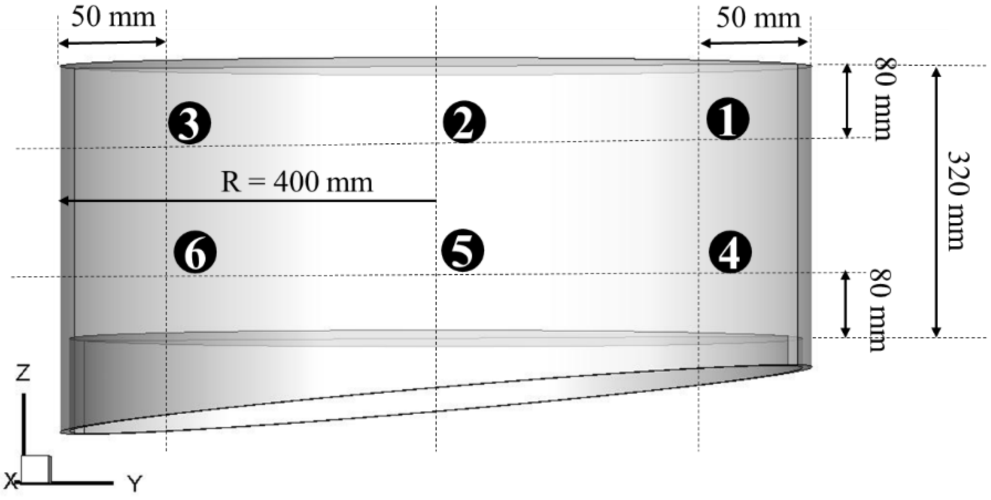

Figure 17: Locations of the evaluation points on the principal plane

At Locations 1 and 2, the gas mixture flow direction, which is inferred by the direction of the droplets with zero radius in Figure 18, is upward, but the droplets with a radius above 18.0 µm flow downwards. Hence the number densities reduce significantly for droplets of a radius above about 23.0 µm at Location 1 and 26.0 µm at Location 2. It is estimated that the 50% volumetric mean diameter (defined such that droplets with diameters smaller than this value constitute 50% of the total volume of aerosol) for these locations are thus approximately 22~23 µm.

At Location 3, all of the droplets flow downwards and the 50% volumetric mean diameter reduces to 18 µm. On the other hand, at Locations 4, 5 and 6, only the droplets with a radius less than 25.0 µm at Location 4 flow upwards, while the others all flow downwards. The number density distribution at Location 4 peaks at 4.92×10^7 g/m^3, which is consistent with the observation in Figure 16 of large droplets accumulating near the pool surface. The 50% volumetric mean diameter of the droplets is 25 µm at Location 5 and 21 µm at Location 6, but increases to above 30 µm at Location 4 with some droplets formed larger than the upper boundary of 50 µm.

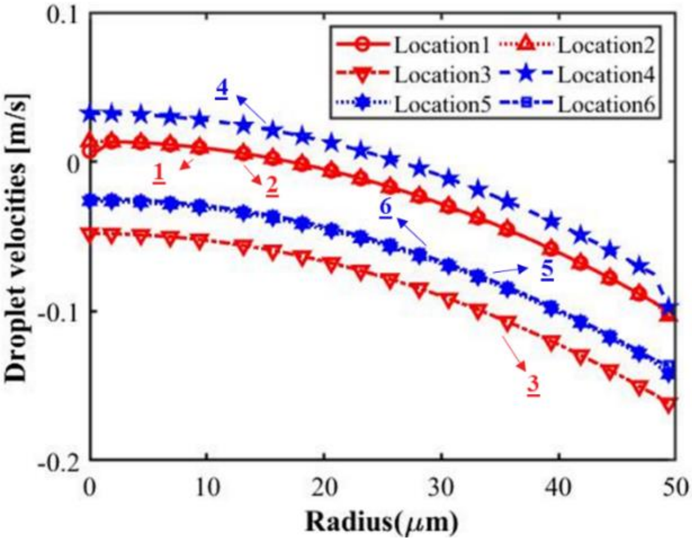

Figure 18: Aerosol velocity variation with droplet size

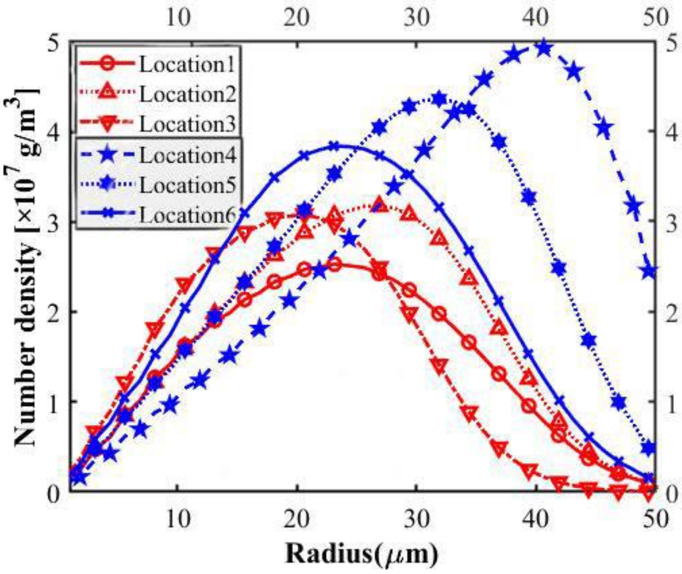

Figure 19: Aerosol number density variation with droplet size

Figure 20 shows the aerosol mass concentration of experiments and simulations with different sodium pool and roof temperatures. The aerosol concentration is measured using the Malvern Instrument and Jet Impactor for a series of pool temperatures between 350 °C and 550 °C and a roof temperature of 120 °C, 160 °C or 200 °C. The Jet Impactor results are always slightly lower than the Malvern Instrument results. Overall, the simulation results agree well with the experiments (closer to those measured using the Malvern Instrument).

Both the experiments and simulations show that the aerosol concentration increases with pool temperature, but there is little influence of roof temperature on aerosol concentration for a fixed pool temperature over the range of conditions covered. In addition to the simulation results shown in Figure 20, two cases were run to evaluate the influence of nucleation mechanism. The spatially averaged aerosol mass concentration with homogeneous nucleation (Case 8) is three orders of magnitude lower than the result shown in Figure 20 with a heterogeneous nucleation rate of 50 $m^{-3}.s^{-1}$. When the nucleation rate is doubled (Case 7), the aerosol concentration increases by approximately 63% to 65 g/m^3 compared to 40 g/m^3 in Case 6 with a pool temperature of 550 °C and roof temperature of 160 °C. The experimental data and simulation results of aerosol mass concentration can be represented by

$$m = 0.0204 \exp(0.0137.T_{pool}) \tag{17}$$

with the R-squared value being 0.955, which can be used to estimate the aerosol concentration under normal operation conditions.

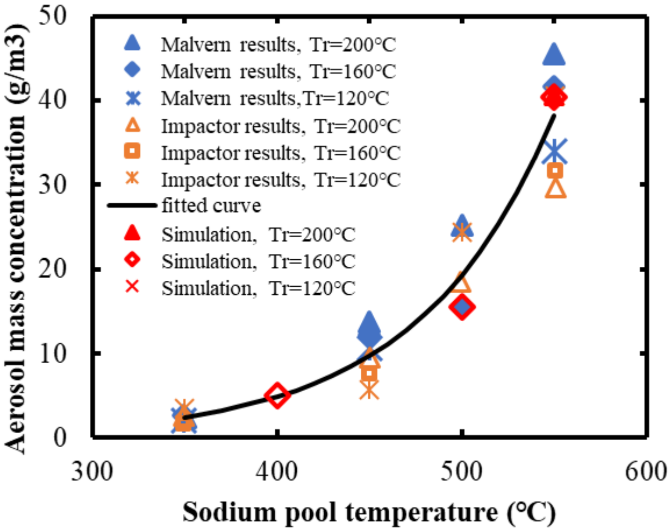

Figure 20: Aerosol mass concentration variation with sodium pool temperature

5 Conclusions

A multi-physics model has been developed to simulate the natural convection and heat transfer of the gas mixture together with aerosol dynamics in the cover gas region. The sectional method is employed for the general dynamics equation of the aerosol allowing for droplet growth by condensation, gravitational settling, Brownian diffusion and convection. This is coupled with the solution of the governing equations for continuity, momentum, energy and mass transfer for the gas mixture with the k-ω SST turbulence model.

This model simulated experiments conducted by Ohira in Japan in early 2000’s and at the University of Manchester in the early 1990s to gain an understanding of the physics in the cover gas region. The major conclusions are as follows:

- The simulation results agree well with the experimental observations in terms of temperature distribution of the cover gas, heat flux through the roof and aerosol mass concentration. Significant differences between the simulation results and experimental data lie in the thermal boundary layer thickness over the top surface and the values of the roof heat flux, which may result from the deposition on the surfaces that occurred in the experiments.
- The flow in the argon cover gas region is dominated by a pseudo 2-D roll-like structure. The main flow direction varies between cases with different roof temperatures, but the structure is stable in each case.
- The droplets however do not follow exactly the large-scale structure of the gas mixture, but instead show smaller circulation cells as a result of gravitational settling. The simulation predicts significant accumulation of droplets above 20 μm radius at the bottom of the domain.
- The pool temperature appears to be a significant factor among these variables, whereas the roof heat flux increases only slightly as roof temperature decreases. A higher nucleation rate causes a higher aerosol concentration, but a lower roof heat flux.
- The nucleation mechanism in this simulation is identified to be heterogeneous as homogeneous nucleation provides an aerosol concentration that is three orders of magnitude lower than the experimentally measured value.

A correlation of the aerosol mass concentration based on the experimental data and simulation results is presented for engineering applications.

The mathematical model has been implemented in Code_Saturne, an open-source finite volume code and therefore can be readily applied to other geometries and other setups of the cover gas region for LMFR designs. The initial development has demonstrated the potential of the model to simulate the aerosol distribution and temperature in the cover gas region, and so could be developed to support the design process.

6 Nomenclature

Symbol	Quantity	SI Unit
C	Cunningham correction factor	
c_p	Specific heat capacity	J/kg/K
D	Diffusivity of gas or aerosol	m^2/s
h	Enthalpy	J/kg
J	Nucleation rate	1/m^3/s
K	Kinetic pre-factor	1/m^3/s
k_B	Boltzmann constant	m^2·kg/s^2/K
l	Mean free path	m
m	Molecular mass	kg
n	Droplet size distribution function	1/m^4
N_A	Avogadro constant	1/mol
P	Pressure	Pa
Q	Latent heat release due to aerosol growth	W
r	Radius	m
R	Universal gas constant	J/mol/K
$\dot{R}$	Growth rate	m/s
S	Supersaturation ratio	
U	Gravitational settling velocity	m/s
$u^{'}$	Velocity fluctuation	m/s
v	Molecular volume	m^3/mol
W	Molecular weight	kg/mol
x	Mole fraction	
Y	Mass fraction	
Γ	Rate of vapour condensation onto the aerosol	kg/m^3/s
λ	Thermal conductivity	J/m/ K
ρ	Density	kg/m^3
σ	Surface tension	N/m
μ	Viscosity of the mixed gas	Pa·s
τ	Relaxation time	s

Subscripts and superscripts

Ar	Argon
g	Gas mixture
G	Gravitational settling
j	j^{th} size bin
Na	Sodium
p	Droplets
sat	Saturation
TS	Terminal settling
*	Critical

7 References

[1] An P., 1992. Studies of Basic Phenomena involved in Radiative Heat Transfer within the Cover Gas Region of Sodium Cooled Fast Breeder Reactors. PhD, University of Manchester.

[2] Anderson A., 1991. Studies of Aerosol Characteristics, Heat Transfer and Mass Transfer with Application to the Cover Gas Region of Sodium Cooled Fast Reactors. PhD, University of Manchester.

[3] Minges J., Chütz W., 1993. NACOWA Experiments on LMFBR Cover Gas Aerosols, Heat Transfer, and Fission Product Enrichment.

[4] Kudo K. and Hirata M., 1977. Sodium vapour deposition onto a horizontal flat plate above liquid sodium surface, 2. Nippon Kikai Gakkai Ronbunshu, 43(368): 1407-1417.

[5] Kudo, K. and M. Hirata, Sodium vapour deposition onto a horizontal flat plate above liquid sodium surface, (3). Nippon Kikai Gakkai Ronbunshu, 1978. 44(379): 1025.1035.

[6] Furukawa O., Furutani. A., Hashimoto Y., Takahashi J., 1979. Heat transfer to rotating plug through cover gas in LMFBR reactor vessel. Japan, Sodium Engineering Division, Power Reactor and Nuclear Fuel Development Corporation: 41.

[7] Wu J. J. and Flagan R. C., 1988. A Discrete-Sectional Solution to the Aerosol Dynamic Equation. Journal of Colloid and Interface Science, 123(2): 339-352.

[8] McGraw R., 1997. Description of Aerosol Dynamics by the Quadrature Method of Moments AU - McGraw, Robert. Aerosol Science and Technology, 27(2): 255.265.

[9] Barnett P. G., Gentry P. J., Jackson J. D. and Tong D. K. W., 1986. Emissivity measurements of liquid sodium and some sodium contaminated steel surfaces. International Atomic Energy Agency (IAEA): 202-219.

[10] Castaing B., Gunaratne G., Heslot F., Kadanoff L., Libchaber A., Thomae S., Wu X.-Z., Zaleski S. and Zanetti G., 1989. Scaling of hard thermal turbulence in Rayleigh-Bénard convection. Journal of Fluid Mechanics, 204: 1-30.

[11] Hattori, N., Furutani, A., Furukawa, O., 1985. Radiative Properties of a Sodium Mist-filled Cover-gas Space. International Working Group on Fast Reactors, Specialists' Meeting on Heat and Mass Transfer in the Reactor Cover Gas. Harwell, England.

[12] Ohira H., 2002. Numerical simulation of aerosol behaviour in turbulent natural convection. Journal of Nuclear Science and Technology, 39(7): 743-751.

[13] Friedlander S. K., 2000. Smoke, dust, and haze: fundamentals of aerosol dynamics, 2nd ed.

[14] Zhou K., Antonio A., Alshaarawi, A., et al. Simulation of aerosol nucleation and growth in a turbulent mixing layer, 26(6): 065106.

[15] Code_Saturne 5.0.0 Theory Guide, 2017, EDF R&D.

[16] Ohira H., 2003. Numerical simulation of aerosol behaviour in turbulent natural convection - Verification of an advanced model. Journal of Nuclear Science and Technology, 40(5): 307-316.

DOCUMENT INFORMATION

Project :	Project FORTE - Nuclear Thermal Hydraulics Research & Development
Report Title :	Aerosol Dynamics in Sodium Cover Gas Region
Client :	Department for Business, Energy and Industrial Strategy (BEIS)

Report No. :	FNC 53798/48653R	**Compiled By :**	Dr X. Huang (University of Sheffield)
Issue No. :	1	**Verified By :**	Professor S. He (University of Sheffield)
Date :	August 2019	**Approved By :**	R. Underhill

Legal Statement

This document has been prepared for the UK Government Department for Business, Energy and Industrial Strategy (BEIS) by Frazer-Nash Consultancy Ltd, and any statements contained herein referring to ‘we’ or ‘our’ shall apply to Frazer-Nash Consultancy and BEIS both individually and jointly.

This document is provided for general information only. It is not intended to amount to advice or suggestions on which any party should, or can, rely. You must obtain professional or specialist advice before taking or refraining from taking any action on the basis of the content of this document.

We make no representations and give no warranties or guarantees, whether express or implied, that the content of this document is accurate, complete, up to date, free from any third party encumbrances or fit for any particular purpose. We disclaim to the maximum extent permissible and accept no responsibility for the consequences of this document being relied upon by you, any other party or parties, or being used for any purpose, or containing any error or omission.

Except for death or personal injury caused by our negligence or any other liability which may not be excluded by an applicable law, we will not be liable to any party placing any form of reliance on the document for any loss or damage, whether in contract, tort (including negligence) breach of statutory duty, or otherwise, even if foreseeable, arising under or in connection with use of or reliance on any content of this document in whole or in part.

This document represents the views of Frazer-Nash Consultancy Limited and does not represent the views of BEIS or the UK Government more widely.

Originating Office: FRAZER-NASH CONSULTANCY LIMITED
The Cube, 1 Lower Lamb Street, Bristol, BS1 5UD
T: +44 (0)117 9226242   F: +44 (0)117 9468924   W: www.fnc.co.uk

Frazer-Nash Consultancy Ltd
The Cube
1 Lower Lamb Street
Bristol
BS1 5UD

T +44 (0)117 9226242
F +44 (0)117 9468924

www.fnc.co.uk

Offices at:
Bristol, Burton-on-Trent, Dorchester,
Dorking, Glasgow, Plymouth, Warrington
and Adelaide